Snow Topography on Undeformed Arctic Sea Ice Captured by an Idealized "Snow Dune" Model

Predrag Popović[1] , **Justin Finkel[2]**, **Mary C. Silber[2,3]**, and **Dorian S. Abbot[1]**

[1]Department of the Geophysical Sciences, University of Chicago, Chicago, IL, USA, [2]Committee on Computational and Applied Mathematics, University of Chicago, Chicago, IL, USA, [3]Department of Statistics, University of Chicago, Chicago, IL, USA

Abstract Our ability to predict the future of Arctic sea ice is limited by ice's sensitivity to detailed surface conditions such as the distribution of snow and melt ponds. Snow on top of the ice decreases ice's thermal conductivity, increases its reflectivity (albedo), and provides a source of meltwater for melt ponds during summer that decrease the ice's albedo. In this paper, we develop a simple model of premelt snow topography that accurately describes snow cover of flat, undeformed Arctic sea ice on several study sites for which data were available. The model considers a surface that is a sum of randomly sized and placed "snow dunes" represented as Gaussian mounds. This model generalizes the "void model" of Popović et al. (2018, https://doi.org/10.1103/PhysRevLett.120.148701) and, as such, accurately describes the statistics of melt pond geometry. We test this model against detailed LiDAR measurements of the premelt snow topography. We show that the model snow depth distribution is statistically indistinguishable from the measurements on flat ice, while small disagreement exists if the ice is deformed. We then use this model to determine analytic expressions for the conductive heat flux through the ice and for melt pond coverage evolution during an early stage of pond formation. We also formulate a criterion for ice to remain pond-free throughout the summer. Results from our model could be directly included in large-scale models, thereby improving our understanding of energy balance on sea ice and allowing for more reliable predictions of Arctic sea ice in a future climate.

1. Introduction

As a hallmark of climate change and a major component of the Arctic environment, Arctic sea ice retreat has garnered much scientific and media attention (Perovich & Richter-Menge, 2009; Stroeve et al., 2007). Predicting the rate of sea ice loss is a significant challenge. The difficulty lies in the fact that sea ice evolution is controlled by many processes that operate on scales ranging from submillimeter to tens of kilometers (Holland & Curry, 1999). Possibly the most notable among these processes is the interaction of ice with environmental energy fluxes mediated by detailed conditions on the ice surface. The presence of snow, water, dirt, or black carbon on the ice surface can drastically change the rate of absorption of solar radiation or the rate of thermal conduction during winter growth (Perovich, 1996). Finding ways to reduce the complexity of modeling ice surface conditions is of great importance for accurately determining the ice energy balance in large-scale models and, therefore, for improving our understanding of the future of sea ice in a changing climate.

Snow insulates the ice (Sturm et al., 2002; Yen, 1981), reflects sunlight (Perovich, 1996), and provides a source of fresh water that collects into melt ponds (Polashenski et al., 2017). The net effect of each of these processes on the heat budget of the ice depends on the spatial distribution of the snow cover. This is important because snow often exhibits significant spatial variability that arises from a multitude of bedforms, most notable of which are meter-scale snow dunes (Filhol & Sturm, 2015; Mather, 1962). Ice covered with patchy snow will, on average, grow faster than if the same amount of snow were spread uniformly, since uniform cover insulates the ice more thoroughly (Sturm et al., 2002). Second, uniform snow cover also protects the underlying ice more from solar radiation than a patchy layer, since even a thin layer of snow can increase albedo significantly (Perovich, 1996). Finally, as snow starts to melt, melt ponds first appear in the regions where there is the least snow (Petrich et al., 2012). For this reason, patchy snow cover leads to melt ponds covering the ice surface sooner, melting more ice. In summary, patchy snow cover will lead to both more ice growth during winter as well as to more ice melt during summer.

Liston et al. (2018) modeled snow on flat ice using a simple statistical approach. They represented the snow surface by smoothing and rescaling an initially random height field to match the measured mean snow depth, its variance, and the horizontal correlation length. Their approach is likely sufficient for many practical applications where snow topography needs to be included. However, it produces some essentially unphysical predictions, such as negative snow depths in cases when snow depth standard deviation is comparable to the mean. Here, we adopt a somewhat similar approach that is physically consistent and reproduces the measurements with high accuracy.

As we mentioned above, snow often exists in meter-scale dunes which are the most prominent features of the snow cover (Filhol & Sturm, 2015; Mather, 1962). In Popović et al. (2018), we considered a simple geometric "void model" which represented these snow dunes as circles and compared it to aerial photographs of melt ponds. These circles had varying size and were placed on a surface randomly and independently of each other, while melt ponds were represented as voids between these circles. Our model was able to reproduce the geometric statistics of melt ponds, such as their size distribution and the fractal dimension as a function of pond size, over the entire observational range of more than 6 orders of magnitude in pond area.

In this paper, we generalize the two-dimensional discontinuous "void model" to a continuous synthetic "snow dune" topography that has a vertical component. We represent snow dunes as mounds of Gaussian form that have a randomly chosen horizontal scale, a height proportional to that scale, and that are placed randomly on the surface. The surface topography is the sum of many such mounds. Like the "void model," this topography accurately describes the horizontal melt pond features, which we take as indirect evidence that it accurately describes the horizontal snow features. We support this by showing that our model fits both LiDAR scans of the premelt snow topography and melt pond data using the same typical horizontal mound scale. The fact that the horizontal scale is so similar is somewhat surprising since the two data sets were recoded in different years, different times of year, and different ice types.

The novel prediction of our continuous topography is a vertical snow depth distribution. By comparing moments of our model distribution to LiDAR measurements of snow depth, we show that our model height distribution is indistinguishable from the measurements for two occasions when the underlying ice was very flat. The one LiDAR measurement on slightly deformed ice showed subtle deviation from our model. Thus, we hypothesize that our model is a highly accurate representation of snow on undeformed ice, while it becomes increasingly inaccurate on deformed ice. The close agreement between snow topography and our model is the main result of this paper. Since our model has only three parameters that are uniquely determined by the mean, variance, and the correlation length of snow depth, it appears that it is only necessary to measure these three quantities to completely characterize the statistics of snow cover on flat, undeformed ice.

After showing the agreement between our model and snow measurements, we consider some applications of our model. First, we consider how spatial variability in snow affects the heat conduction through the ice during winter ice growth. Sturm et al. (2002) conducted measurements of snow conductivity, k_s, on deformed multiyear ice, and found that k_s inferred from ice growth is $\sim$2.4 times higher than k_s inferred from direct measurements. They found that about 40% of the increase can be explained by snow and ice geometry and that horizontal heat transport, typically neglected in large-scale models, likely contributes significantly. To understand whether these conclusions also hold for undeformed ice, we solve a three-dimensional heat equation within the ice assuming that the snow cover is well described by our "snow dune" model. We develop a simple analytic equation to determine the heat flux conducted through the ice given a set of physical parameters. Contrary to Sturm et al. (2002), our model shows a negligible horizontal heat transport. Moreover, our model shows a smaller increase in heat conduction than Sturm et al. (2002). This disagreement could be due to the fact that our model assumes undeformed ice, while the field measurements of Sturm et al. (2002) were made on deformed ice.

Next, we consider the effect of snow topography on early melt pond development. Using the fact that our model height distribution is well fit with a gamma distribution, we write an analytic evolution equation for melt pond coverage during an early stage when ice is impermeable. This equation for melt pond evolution enables us to understand how early-stage melt pond growth depends on measurable environmental parameters. Moreover, it allows us to derive a simple condition that distinguishes whether ice will remain pond-free throughout the summer based on snow depth, variance, density and melt rate.

Comparing the "void" model,
"snow dune" model, and real melt ponds
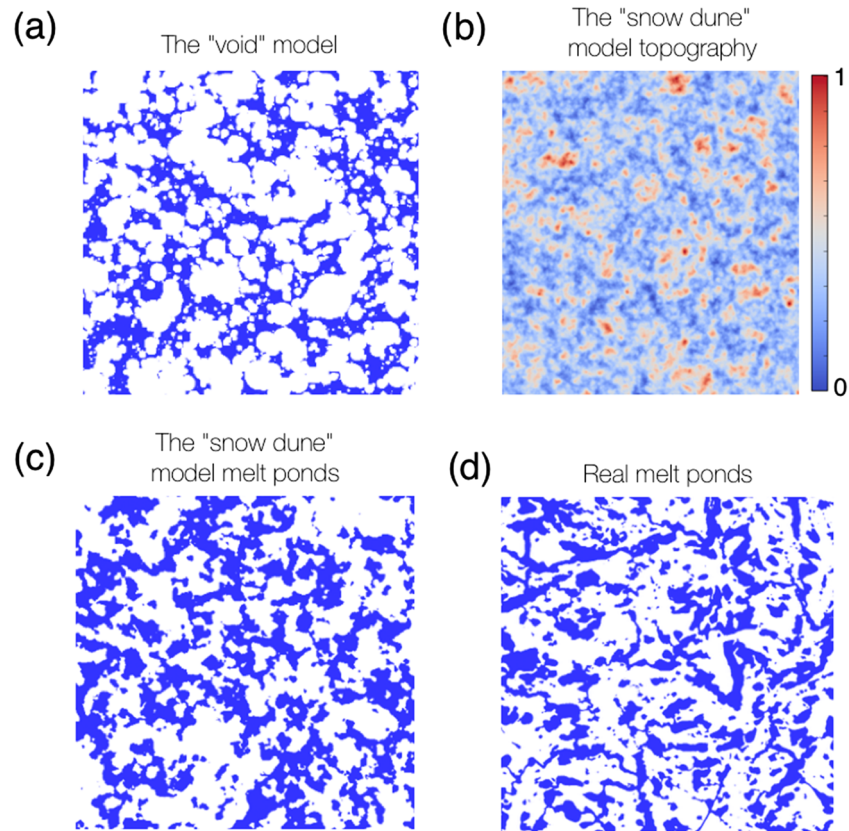
Figure 1. (a) A realization of the "void model." Figure is taken from Popović et al. (2018). (b) Synthetic "snow dune" topography. Red colors indicate topographic highs, while blue colors indicate topographic lows. The upper bound on the scale bar, here set to 1, is arbitrary. (c) Ponds on a "snow dune" topography. (d) A binarized image of a real melt pond photograph taken on 14 August during the HOTRAX mission.

This paper is organized so that the new results are presented in the main text, while confirming previous results about melt ponds on our topography and mathematical details are left for the supporting information (SI). In section 2, we describe our model of the "snow dune" topography. Next, in section 3, we describe the analytical properties of our model such as the dependence of moments and the correlation function on model parameters. Then, in section 4, we compare our model with the measured snow topography. In section 5, we apply our "snow dune" model to determine the conductive heat flux through the ice. Next, in section 6, we use our model to investigate melt pond evolution on flat impermeable ice. Finally, in section 7, we discuss the implications of our results for large-scale studies, and in section and 8, we conclude. In SI section S1, we confirm that ponds on the synthetic "snow dune" topography accurately reproduce the geometric statistics of real melt ponds during late summer. In the subsequent SI sections, we prove the mathematical results and show that our model predictions are robust against details such as the shape of the mounds or mound radius.

2. The Synthetic "Snow Dune" Topography

In this section we will describe our synthetic "snow dune" topography. The entire rest of the paper hinges on this topography.

In Popović et al. (2018), we developed a simple geometric model where snow dunes were represented as overlapping circles of varying size placed randomly and independently of each other on the ice surface,

while melt ponds were represented as voids between these circles. We then compared the statistical properties associated with this simple geometric model with observations of late-summer melt ponds. We found a remarkable agreement between various statistics of real and model melt ponds: By tuning only two model parameters, the model matched the measured pond area distribution, the pond fractal dimension as a function of pond area, and two correlation functions that describe pond size and connectedness, over the entire observational range of nearly 7 orders of magnitude in pond area. A realization of this model is shown in Figure 1a.

Motivated by the success of the "void model" in capturing the conditions on the ice surface, we set about to generalize it to a three-dimensional "snow dune" topography that has an additional vertical component and can, thus, be compared with a pond-free snow-covered ice surface. We will show that, in addition to reproducing melt pond features, the "snow dune" model also matches the observed snow depth distribution and correlation function on flat, undeformed ice.

To generalize the "void model" to a continuous topography, we replace circles with mounds that have a vertical profile. The mounds have a Gaussian shape

$$h(\mathbf{x}) = h_m e^{-(\mathbf{x} - \mathbf{x}_0)^2/2r^2},$$ (1)

where $h(\mathbf{x})$ is the height of the mound at a point $\mathbf{x}$ on the surface, $\mathbf{x}_0$ is the location of the center of the mound, r is the horizontal scale, and h_m is the maximum height of the mound. Mounds are placed randomly, that is, $\mathbf{x}_0$ can be anywhere on the surface with equal probability. The horizontal scale, r, of each mound is randomly chosen from an exponential probability distribution, f_r

$$f_r(r) = \frac{1}{r_0} e^{-r/r_0},$$ (2)

where r_0 is the typical horizontal scale of the mounds. This distribution is the same as the distribution of circle radii in the "void model" of Popović et al. (2018), and we chose it mainly due to its simple form and the fact that it depends on a single parameter, r_0. Otherwise, the choice of this distribution is arbitrary and does not affect the main conclusions of our model so long as it is not long tailed. To prevent having unrealistically narrow and high mounds, we prescribed the height of each mound, h_m, to be proportional to its horizontal scale, $h_m = h_{m,0} r/r_0$, where $h_{m,0}$ is the typical mound height that we prescribe as an independent model parameter. The topography is then a sum of N such mounds placed on an initially flat surface

$$h_{\mathrm{SD}}(\mathbf{x}) = \sum_{i=1}^{N} h_{m,0} \frac{r_i}{r_0} e^{-(\mathbf{x} - \mathbf{x}_{0_i})^2/2r_i^2},$$ (3)

where $h_{\mathrm{SD}}(\mathbf{x})$ is the height of the "snow dune" topography at location $\mathbf{x}$. A realization of this topography is shown in Figure 1b. Ponds that form on this surface after cutting it with a horizontal plane are shown in Figure 1c. This is shown alongside a realization of the "void model" (Figure 1a) and a binarized image of real melt ponds (Figure 1d).

There are three parameters in this model. These are the typical horizontal mound scale, r_0, the density of mounds, ρ, placed within the domain of size L, $\rho \equiv N \frac{r_0^2}{L^2}$, and the typical mound height, $h_{m,0}$. The first two of these parameters, r_0 and ρ, also enter the "void model."

Although our model mounds bare some resemblance with real snow dunes, our model is not accurate on the scale of individual dunes. In particular, snow dunes are certainly not Gaussian-shaped, they show strong anisotropy, the distribution of dune sizes is likely not exponential, and dunes sometimes form semiregular lattices, which violates our assumption of random placement (Filhol & Sturm, 2015; Kochanski, Anderson, et al., 2019; Kochanski, Defazio, et al., 2019; Sharma et al., 2019). In SI section S2.3, we show that aggregate, radially averaged statistical properties of the snow surface that we consider in this paper do not depend on most of these details. We note, however, that the random placement assumption is important for the conclusions we make, so our model can be useful for large-scale studies only if snow surfaces that strongly violate this assumption do not occur often in nature.

3. Statistics of the Synthetic "Snow Dune" Topography

Here, we describe the statistics of the "snow dune" model that we will use later. In particular, we first show how the mean, variance, and correlation length depend on model parameters r_0, ρ, and $h_{m,0}$. We then show a formula to calculate all of the moments of the height distribution of the topography. Finally, we compare the height distribution of the "snow dune" topography with a gamma distribution. We derive all of the results in this section in SI section S2. All of these results follow directly from the definition of the "snow dune" model we described in section 2.

First, we find that the mean, $\langle h_{SD} \rangle$, and variance, $\sigma^2(h_{SD}) = \langle (h_{SD})^2 \rangle - \langle h_{SD} \rangle^2$, of the topography depend on the typical mound height, $h_{m,0}$, and the density of mounds, ρ, as

$$\langle h_{SD} \rangle = 12\pi h_{m,0}\rho, \quad \sigma^2(h_{SD}) = 24\pi h_{m,0}^2 \rho. \tag{4}$$

In fact, we can explicitly find every moment of the topographic height distribution, $\langle (h_{SD})^n \rangle$, by knowing the previous moments and using the recursion formula (see SI section S2 for derivation)

$$\langle (h_{SD})^n \rangle = 2\pi\rho \sum_{j=1}^{n} \binom{n-1}{n-j} \frac{(j+2)!}{j} h_{m,0}^j \langle (h_{SD})^{n-j} \rangle. \tag{5}$$

Equations 4 also follow from this formula.

Next, we define the height correlation function, $C_h(\mathbf{l})$, as

$$C_h(\mathbf{l}) \equiv \frac{\langle h_{SD}(\mathbf{x}) h_{SD}(\mathbf{x}+\mathbf{l}) \rangle - \langle h_{SD} \rangle^2}{\sigma^2(h_{SD})}, \tag{6}$$

where $\mathbf{l}$ is a horizontal displacement of the topography. Below, we will use the boldface notation, $\mathbf{l}$, to denote the vector displacement and we will use the italic notation, l, to denote the magnitude of this displacement. The correlation function quantifies how much the surface height at $\mathbf{x}$ is correlated with the surface height at $\mathbf{x}+\mathbf{l}$. If the surface is isotropic, C_h only depends on the magnitude of the displacement vector, l. We can then define the correlation length, l_0, as the distance at which C_h falls by a factor of e. Beyond l_0, features on the topography can be considered approximately uncorrelated. Using these definitions, we find that C_h and l_0 depend on the horizontal mound scale, r_0, of an isotropic "snow dune" model as (see SI section S2 for derivation)

$$C_h(l) = \frac{1}{24}\int_0^\infty z^4 e^{-z - l^2/(2r_0 z)^2} dz, \tag{7}$$

$$l_0 = r_0 \xi_0, \tag{8}$$

where $\xi_0 \approx 9.3689...$ is a number that can be estimated to arbitrary precision by inverting $C_h(l_0) = 1/e$ using Equation 7. The mean, variance, and the correlation length are all measurable properties of real topographies. This means that computing these quantities from measurements lets us unambiguously choose the model parameters limited only by the accuracy of those measurements.

Since we can find all of the moments of the "snow dune" topography using Equation 5, we can fully determine its height distribution. However, it is impractical to do this, and, for practical purposes, we now show that the height distribution of the "snow dune" topography is well fit with a gamma distribution. The two distributions are not the same, as can be seen by comparing their moments (see SI Figure S2). However, they are qualitatively very similar, and the differences between them arise from arbitrary choices in our model such as the exponential distribution of radii of the snow dunes, Equation 2, and the linear relationship between the mound radius and height. We describe the relationship between the height distribution of the "snow dune" topography and the gamma distribution in detail in SI section S2.

A gamma distribution has the form

$$f_\Gamma(h) = \frac{1}{\Gamma(k)h_0^k} h^{k-1} e^{-h/h_0}, \tag{9}$$
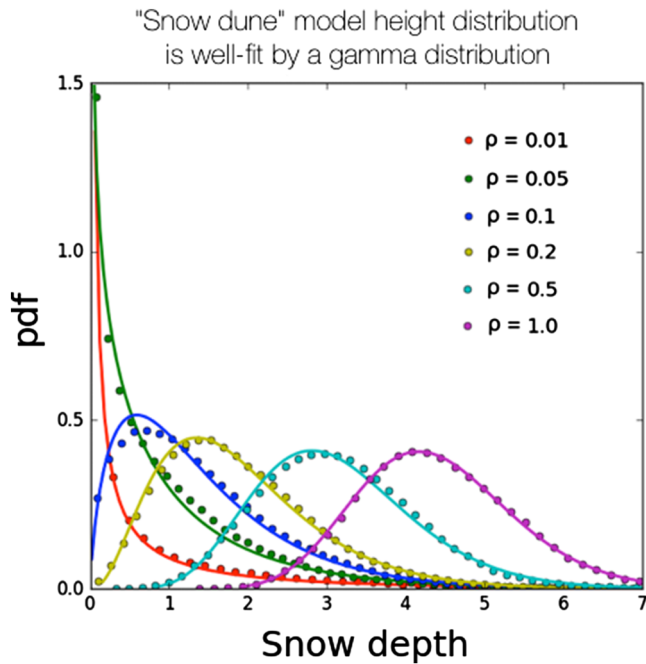
Figure 2. Dots represent the height distribution of the "snow dune" topography for different densities of mounds, ρ. Solid lines represent fits using a gamma distribution. Units of snow depth here are arbitrary. Note that the LiDAR measurements we consider in section 4 range from $\rho \approx 0.2$ to $\rho \approx 0.5$, a much smaller range than we investigated here.

where h_0 is a scale parameter, k is a shape parameter, and $\Gamma(x)$ is a gamma function. The two parameters of the gamma distribution, h_0 and k, are related in a simple way to the mean and variance of the distribution, $\langle h \rangle$ and $\sigma^2(h)$

$$k = \frac{\langle h \rangle^2}{\sigma^2(h)}, \quad h_0 = \frac{\sigma^2(h)}{\langle h \rangle}. \quad (10)$$

Both of these parameters are therefore uniquely determined by the typical height and density of mounds through Equations 4. In particular, we find that the scale parameter, h_0, scales linearly with the typical height of mounds, while the shape parameter, k, scales linearly with the density of mounds,

$$h_0 = 2h_{m,0}, \quad k = 6\pi\rho. \quad (11)$$

In Figure 2, we show height distributions for synthetic topographies with varying spatial densities of mounds, ρ, with the variance, $\sigma^2(h_{SD})$, kept fixed. We can see that varying ρ changes the shape of the distribution and that a gamma distribution can fit the height distribution well for all choices of ρ. To quantify the quality of the fit, we use the Kolmogorov-Smirnov (KS) statistic, that is, the maximum distance between the empirical and theoretical cumulative distributions. The fit is typically considered good if this statistic is below 0.05. We find that for all choices of ρ, the maximum distance between the cumulative "snow dune" height distribution and the best fit gamma distribution is below 0.05, and ranges between 0.03 for $\rho = 0.01$ to 0.006 for $\rho = 1$, generally decreasing for increasing ρ. Our "snow dune" model height distribution compares similarly well with a gamma distribution according to other metrics such as the Kuiper or the Cramér-von Mises metrics.

In SI section S2.3, we compare different variants of our model that include anisotropy, different dune shapes, and different distributions of mound sizes. There, we show that moments of the height distribution as well as the radially averaged correlation function are insensitive to these details. Namely, these alterations were only able to change the numerical prefactors in equations that relate model parameters to measurable quantities, such as 12π and 24π in Equations 4 or ξ_0 in Equation 8. Since our conclusions regarding heat conduction and melt pond evolution that we discuss later in the paper only rely on these invariant statistics, they should also be robust to detailed model assumptions on the scale of individual dunes. We caution, however, that certain phenomena, such as the wind stress, may explicitly depend on specifics such as snow anisotropy. In such a case, additional parameters in the model describing these details would be required.

4. Measured Snow Topography

The synthetic "snow dune" topography is meant to represent the height of snow relative to the flat underlying ice. Therefore, the height distribution of the "snow dune" topography should correspond to the premelt snow depth distribution. Here, we will compare the statistics of the synthetic "snow dune" topography to detailed LiDAR measurements of premelt snow topography made by Polashenski et al. (2012).

During their field expedition, Polashenski et al. (2012) performed detailed LiDAR scans of the surface topography within a 100 m × 200 m region on multiple dates in 2009 and 2010 near Barrow, Alaska. During 2009, Polashenski et al. (2012) monitored two locations separated by about 1 km from each other, one in the north (2009N) and one in the south (2009S). In 2010 they monitored only one location. In Figure 3a we show an example of such a measurement, which shows the height of snow before the start of the melt season, and compare it to a randomly generated "snow dune" topography (Figure 3b). Assuming that the underlying ice is flat and the premelt ice is fully covered with snow, the LiDAR-estimated height in Figure 3a represents the snow depth plus some reference height. Therefore, to compare with the "snow dune" topography, we estimated the snow depth from these LiDAR scans by subtracting the minimum LiDAR elevation from

"Snow dune" model matches the observed snow-depth distribution on flat ice
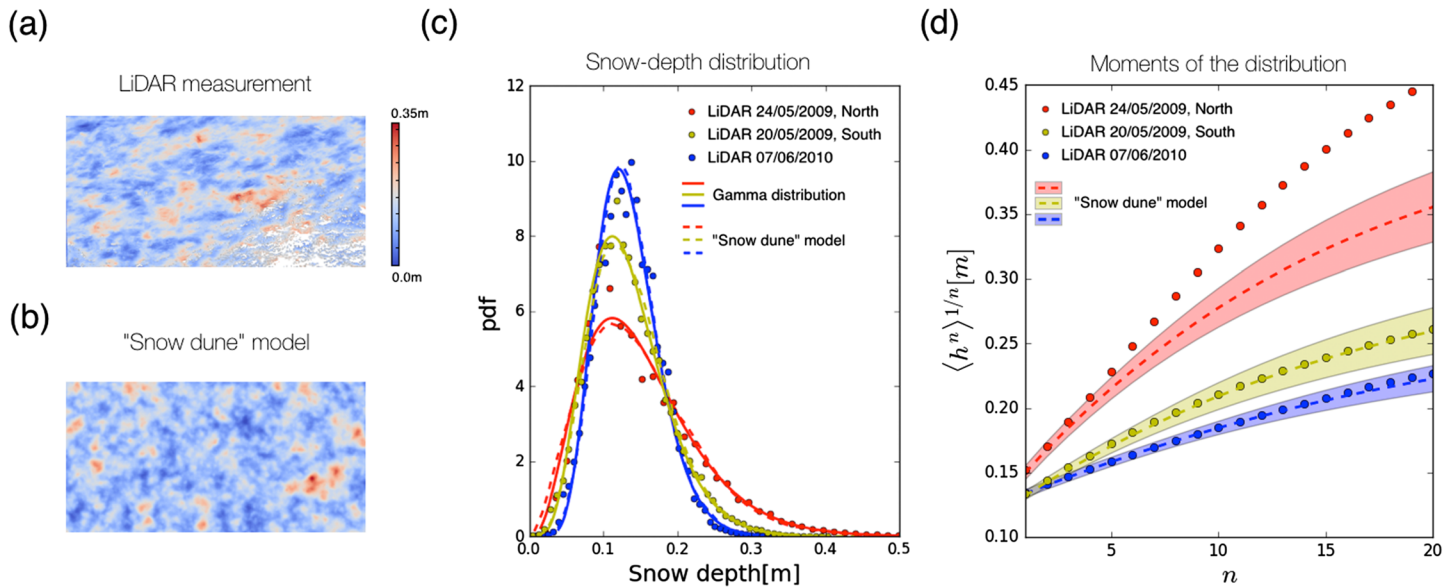
Figure 3. (a) LiDAR measurement of the premelt snow topography by Polashenski et al. (2012) in early June 2010. (b) A realization of synthetic "snow dune" topography. The density of mounds was chosen such that the height distribution of the synthetic topography corresponds well to the measured snow depth distribution. (c) Dots represent snow depth distribution estimated using LiDAR measurements for two different years. Solid lines are gamma distributions with parameters estimated based on the mean and variance of the measurements. Dashed lines are the corresponding "snow dune" topography height distributions and are nearly indistinguishable from the solid lines. (d) Moments of the height distribution. The horizontal axis is the moment order, n, while the vertical axis is the nth root of the nth moment. Dots represent moments of the measured snow topography. The thick dashed lines represent the mean moments across an ensemble of 50 randomly generated "snow dune" topographies on the domain of the same size as the measurements. The colored shadings represent one standard deviation from the mean on that ensemble.

the rest of the scan. We show the snow depth distribution for the three LiDAR scans in Figure 3c, and we show the moments of these distributions in Figure 3d. We estimate the height correlation function for these three measurements in Figure 4. The data from Polashenski et al. (2012) are freely available online (at https://chrispolashenski.com/data.php).

To see whether the snow depth distribution of these measurements conforms to the predictions of our model and a gamma distribution, we inferred parameters $h_{m,0}$ and ρ using Equations 4 and parameters of the gamma distribution, k and h_0, using Equations 10 based only on measured mean snow depth and snow depth variance. We show the statistics of measured topographies along with model and gamma distribution parameters in Table 1. The solid lines in Figure 3c show a gamma distribution with parameters chosen in this way, while the dashed lines show a height distribution of the synthetic "snow dune" topography. We can see that in all cases, the measured snow depth distribution agrees well with our model and a gamma distribution, with a Kolmogorov-Smirnov (KS) statistic remaining at or below 0.03 in all cases.

We can gain a better understanding of both the measured and the synthetic snow depth distributions by looking at their moments. Higher order moments describe the more and more detailed structure of the probability distribution. This is precisely why we can use these higher order moments to distinguish between similar, but subtly different distributions. In Figure 3d, we compare moments of the measured snow topography and randomly generated "snow dune" topographies. Higher order moments depend on the domain size, resolution, and the particular realization of the topography. For this reason, to get the moments of the simulated "snow dune" topographies, we created an ensemble of 50 randomly generated topographies with the same resolution and domain size as the measurements. For each realization, we then found the root moments, $\langle h^n \rangle^{1/n}$. Dashed lines in Figure 3d show the mean and one standard deviation of the root moments over this 50-member ensemble. We used the model parameters shown in Table 1.

For the 2010 and 2009S measurements, all of the measured moments fall squarely within the range of values obtained with an ensemble of simulated "snow dune" topographies. In fact, we tested the first 150 moments

The model correlation function matches the observations
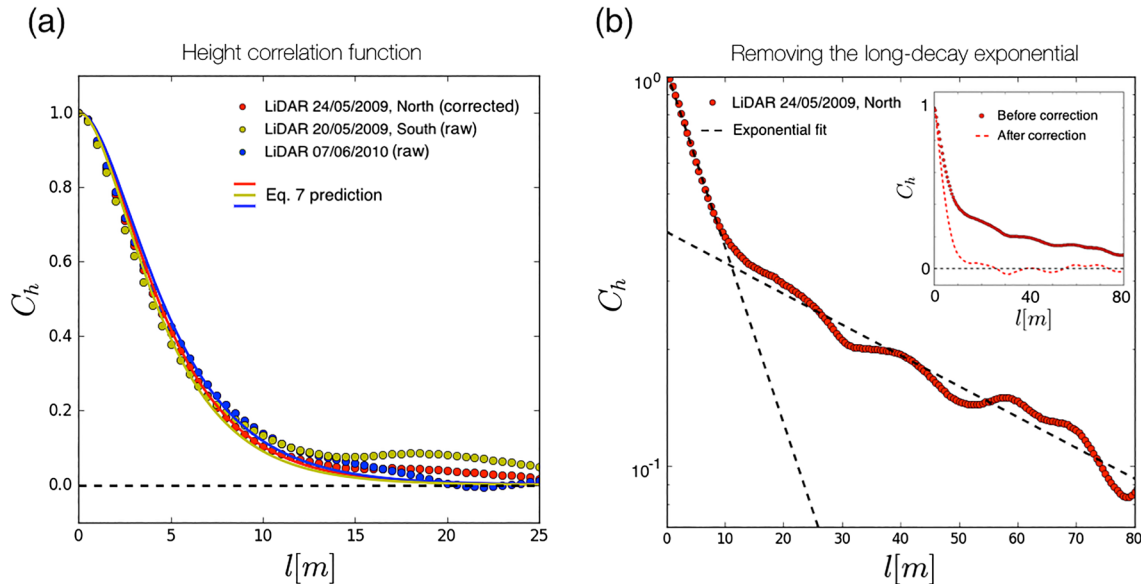
Figure 4. (a) Height correlation functions. Dots represent measurements, and the solid lines represent predictions for the "snow dune" model using Equation 7. Correlation functions for 2010 and 2009S measurements (yellow and blue dots) were calculated from raw data. Correlation function for the 2009N measurement was corrected by removing a long-decay exponential. The raw 2009N data are shown in Panel b. (b) Correction for the 2009N correlation function. Dots represent C_h calculated from raw data on a semilog plot. The two black dashed lines are exponential fits to the short-decay and long-decay portions of C_h. Inset shows C_h before (red dots) and after (red dashed line) removing the long-decay exponential on a linear plot.

for these two measurements, and found that this agreement holds throughout. This means that realizations of the "snow dune" topography that have *exactly* the same height distribution as the measurements are common. We can therefore conclude that the snow depth distribution for 2010 and 2009S measurements is indistinguishable from the "snow dune" height distribution! This agreement is, however, not observed for 2009N measurements—moments of measured snow depth distribution are consistently higher than those of the simulations and no randomly generated "snow dune" topography has high order moments that match the measurements. This difference is subtle, which is why we could not observe it using the KS statistic, and for most practical uses that require only a snow depth distribution it is unlikely to be important. Nevertheless, it constitutes a real observable difference between our model and the 2009N measurements, and shows that there exist features in real data that our model cannot capture. We return to explaining this difference below.

Next, we describe the height correlation function, $C_h(l)$, for measurements and the model. We find the LiDAR $C_h(\mathbf{l})$ using Equation 6. Due to prevailing winds, snow on sea ice often shows a strong preferential orientation, with snow dunes elongated along the direction of the wind (Petrich et al., 2012). We observe this in the measured $C_h(\mathbf{l})$, which we find to depend on the direction of the displacement vector, $\mathbf{l}$. Such anisotropy can be included in our model by elongating the mounds along a particular axis. However, to keep our discussion as simple as possible, we chose to keep our model isotropic. Thus, to obtain a measured correlation function that depends only on the magnitude of $\mathbf{l}$, we average the measured $C_h(\mathbf{l})$ over all directions of $\mathbf{l}$. Then, we find the correlation length, l_0, the distance at which the measured $C_h(l)$ falls off by a factor of e, and relate it to the model parameter r_0 according to Equation 8 (see Table 1). We show the measured and the theoretical $C_h(l)$ calculated according to Equation 7 in Figure 4.

Again, we find that 2010 and 2009S measurements agree very well with model predictions (Figure 4a). However, 2009N shows some disagreement with the model. The height correlation function calculated from raw 2009N data is shown in Figure 4b. It first decays quickly, and then the decay slows down, with features on the surface remaining correlated across the domain. By plotting C_h on a semilog plot, we find that it is approximately a sum of two exponentials—one with a short-decay length and another with a long-decay

Table 1
Statistics of the LiDAR Measurements and Model Parameters Inferred From Them

	$\langle h \rangle$	$\sigma(h)$	l_0	$h_{m,0}$	ρ	r_0	h_0	k	KS
2009N	15.2 cm	7.8 cm	5.5 m	2.0 cm	0.20	0.59 m	4.0 cm	3.8	0.03
2009S	13.4 cm	5.4 cm	5.2 m	1.1 cm	0.33	0.56 m	2.2 cm	6.2	0.01
2010	13.4 cm	4.3 cm	5.8 m	0.7 cm	0.53	0.61 m	1.4 cm	9.9	0.03

Note. The KS statistic was calculated with respect to the gamma distribution.

length comparable to the domain size. We get good agreement with the model after removing this long-decay exponential. To do this, we fit an exponential function to C_h for $l > 20$ m. We then subtract this exponential from the whole C_h and rescale so that $C_h(0) = 1$. The result is a corrected correlation function, shown as the red dots in Figure 4a and the dashed line in the inset of 4b. The result of this correction does not depend strongly on the choice of the cutoff length for the exponential fit so long as this length is large enough. The correlation length, l_0, and the model parameter r_0 reported in Table 1 for 2009N data correspond to this corrected correlation function.

In Popović et al. (2018) and SI section S1, we calculated similar correlation functions for melt pond images taken during 1998 and 2005. There, we similarly observed correlation functions with two decay lengths—one comparable to the size of melt ponds and another comparable to the size of the images. In Popović et al. (2018), we attributed the long-decay length to differences in ice properties between different ice floes and large-scale deformation features such as ridges. A match between the model and the data could only be achieved after removing this long-decay length by a procedure analogous to the one we described above.

Here, we again suggest that the long-decay length comes from variability in the underlying properties of the ice. In fact, we believe that all of the differences between 2009N measurements and the model can be explained by this variability in the underlying ice properties. Polashenski et al. (2012) note that the 2009N site had ice that finger rafted early in the growth season and contained some lightly rubbled ice, while the 2009S site had very flat ice. They did not comment on ice conditions during 2010 measurements. To test whether our model is consistent with variable ice properties across the domain, we created a "snow dune" topography where one half of the domain had higher $h_{m,0}$ and ρ than the other half, but together both parts had the same mean and variance as the measured 2009N topography. In this experiment, the model correlation function obtained a long-decay length comparable to the domain size. Moreover, we found that we can choose the parameters in the first half of the domain such that all of the moments of the model height distribution match the moments of the 2009N data. Therefore, our model is consistent with the 2009N data if we assume that 2009N data contains regions with different underlying ice properties. We note that even though there exists an observable difference between the snow depth distribution of 2009N and our model, it is very small and would likely not significantly change the ice evolution in a large-scale model. Nevertheless, it hints that highly deformed ice may in fact significantly deviate from our model.

In SI section S1, we compare melt ponds on the synthetic "snow dune" topography with melt pond data derived from images taken during 1998 and 2005. These images cover a much larger area than the LiDAR scans we considered here. Each melt pond image covers an area of roughly 1 km^2 as opposed to 0.02 km^2 covered by the LiDAR scans. As in Popović et al. (2018), we find an agreement between the observed and model melt ponds. To match the melt pond statistics, we had to choose $r_0 \approx 0.6$ m in the model for both 1998 and 2005 ponds, in close agreement with r_0 we find here from the height correlation functions of the premelt height topographies (see Table 1). In all three measurements of the LiDAR topography, we found r_0 within at most several cm from $r_0 = 0.6$ m. We take this as evidence that melt ponds are controlled by the premelt snow topography and that the "snow dune" model may be meaningfully extended to at least the kilometer scale.

We will make several final notes to end this section. First, we note that since $r_0 \approx 0.6$ m in observations for four different years and multiple locations and ice types, the horizontal scale of the snow features seems to be a robust property of the snow cover. For this reason, future models that require a representation of snow may be able to keep the correlation length $l_0 \approx 5.6$ m fixed, and only keep track of mean snow depth and variance in order to represent snow in a principled way. Second, we note that distributions other than a gamma distribution that have been used to model the snow depth, such as normal (Liston et al., 2018) or

lognormal (Landy et al., 2014), can also often fit the measurements well. For example, a lognormal distribution passes the KS test for all three LiDAR measurements, while a normal distribution passes the KS test for 2010 measurements. However, these distributions cannot qualitatively capture the height distribution of the synthetic "snow dune" topography for all values of the density of mounds, ρ, while a gamma distribution can. For small ρ (large ratio of standard deviation to mean), a normal distribution predicts a significant fraction of negative observations, while a lognormal distribution predicts a fat tail at large h. Since the "snow dune" model so closely reproduces both the LiDAR and melt pond measurements, we believe that a distribution that is qualitatively consistent with the predictions of the "snow dune" model is a more justified model for a snow depth distribution that would fit the measurements over a wider parameter range. Finally, we note that Filhol and Sturm (2015) and Kochanski, Anderson et al. (2019) observed an approximately linear relationship between snow dune height and width for dunes that formed on snow-covered lake ice, tundra, and mountain landscapes. Our model prescription is therefore consistent with these observations. The data in Kochanski, Anderson et al. (2019) was quite noisy, but Filhol and Sturm (2015) reported a slope of the height-width relationship ranging from about 0.03 to 0.06. We can estimate the mound aspect ratio in our model as $h_{m,0}/r_0$ and compare it with Filhol and Sturm (2015). From Table 1, we find that the aspect ratio of mounds in our model varies between 0.01 for 2010 measurements and 0.03 for 2009N measurements. These estimates are lower but broadly of the same order of magnitude as those of Filhol and Sturm (2015), which suggests that mounds in our model are at least broadly consistent with dunes observed in the field, although not in detail.

5. Heat Transport Through the Ice

In this section we will consider the application of our model to heat conduction through the ice. Sturm et al. (2002) conducted measurements on deformed multiyear ice, and concluded that the conductivity of snow inferred from large-scale ice growth is roughly 2.4 times higher than the conductivity of snow measured on site. They ascribed a significant portion of this difference to spatial variability of snow depth and also suggested that a significant fraction of heat is transported horizontally. Motivated by their study, here we investigate the extent to which these conclusions also apply to undeformed ice. We consider a full three-dimensional model of heat conduction to determine how much heat is extracted through undeformed ice with variable snow cover.

To model heat conduction, we assume that ice is a block of uniform thickness, H, that ice and snow have fixed conductivities, k_i and k_s, that the snow cover is well described by our "snow dune" model, that the temperature at the ice-ocean interface is fixed at the freezing point of salt water, T_f, and that the temperature of the snow surface is fixed at the temperature of the atmosphere, T_a, and that the temperature field within the ice and snow is in a steady state. Additionally, we assume that heat is transported purely vertically in the snow (but not necessarily in the ice), which is reasonable, since snow cover is typically thin compared to its horizontal correlation length. Finally, we impose periodic boundary conditions in the horizontal directions. Some of the assumptions above may not be realistic. For example, ice is almost certainly not a uniform block, snow conductivity, k_s, typically has large variations in both the horizontal and the vertical, and the system is likely not in a steady state since the conditions in the atmosphere change faster than snow and ice can adjust. For these reasons, our investigation here should be considered to be a first-order estimate of the effects of snow geometry.

In SI section S3, we develop relations for the mean conductive heat flux through the ice, F_c, under the assumptions above. In particular, starting from Laplace's equation for heat conduction and using the fact that our "snow dune" model is fully characterized by the mean, variance and the correlation length of the snow surface, we show that F_c must be of the form

$$F_c = F_0 \Phi(\eta, \Sigma, \Lambda),\tag{12}$$

$$F_0 \equiv k_i \frac{T_f - T_a}{H}, \quad \eta \equiv \frac{k_i}{k_s}\frac{\langle h \rangle}{H}, \quad \Sigma \equiv \frac{\sigma(h)}{\langle h \rangle}, \quad \Lambda \equiv \frac{l_0}{H},\tag{13}$$

where Φ is a nondimensional flux that is determined by a nondimensional snow depth, η, a nondimensional snow roughness, Σ, and a nondimensional correlation length, Λ. The dimensional quantity F_0 is

Table 2
Nondimensional Parameters of the Snow Surface for the LiDAR Measurements of Polashenski et al. (2012) Assuming an Ice Thickness of H=1 m, Conductivity of Fresh Ice k_i=2.034 W m^{-1} K^{-1} (Untersteiner, 1964), Snow Conductivity Estimated by Sturm et al. (2002), k_s=0.14 W m^{-1} K^{-1}, and Duration of Stage I of Pond Evolution T=5 Days

	η	Σ	Λ	Φ_u	Φ_v	Φ_h	Φ	$(\Phi-\Phi_u)/\Phi$	ω
2009N	2.2	0.5	5.5	0.31	0.35	0.38	0.35	0.11	1.7
2009S	1.9	0.4	5.24	0.34	0.37	0.39	0.37	0.07	1.7
2010	1.9	0.3	5.75	0.34	0.36	0.37	0.36	0.04	1.5

the heat flux conducted through the ice with no snow on top, so the function $\Phi \leq 1$ represents the fraction of this flux that is conducted when snow is present. After showing this, in SI section S3, we show that the heat conduction problem can be explicitly solved if $\Lambda \to \infty$ (when heat transport is purely vertical), and when $\Lambda \to 0$ (when the horizontal heat transport dominates). Knowing these two limits, we then numerically solve the heat conduction problem for various combinations of the parameters η, Σ, and Λ and show that the function Φ is approximately equal to

$$\Phi(\eta, \Sigma, \Lambda) \approx \Phi_v + \frac{\Phi_h - \Phi_v}{(1 + c\Lambda)^2}, \tag{14}$$

$$\Phi_v \equiv \int_0^\infty \frac{\widetilde{f}_\Gamma(z, \Sigma)}{1 + z\eta} dz \qquad \text{(purely vertical heat transport)}, \tag{15}$$

$$\Phi_h \equiv \frac{1}{1 + \eta(1 - \Sigma^2)} \qquad \text{(dominant horizontal heat transport)}, \tag{16}$$

where $c \approx 0.83$ is a numerical constant, Φ_v is the nondimensional flux if vertical heat transport dominates, and Φ_h is the nondimensional flux if horizontal heat transport dominates. Φ_h is an upper bound on heat flux given parameters η and Σ. The gamma distribution $\widetilde{f}_\Gamma$ in Equation 15 is normalized to have a mean equal to 1, and is consequently only a function of Σ with the parameters $k = \Sigma^{-2}$ and $h_0 = \Sigma^2$. Equation 16 is only valid for $\Sigma < 1$. If $\Sigma > 1$, we have that $\Phi_h = 1$ so that, if $\Lambda \to 0$, the heat is conducted as if there were no snow on top of the ice, $F = F_0$.

To quantify how much ice growth is due to snow depth variability, we also consider the nondimensional flux assuming a uniform snow cover, $\Phi_u \equiv \frac{1}{1 + \eta}$. The fraction of ice growth that can be attributed to snow depth variability can then be estimated as $\frac{\Phi - \Phi_u}{\Phi}$. We show the estimated values of all of the nondimensional parameters discussed above for the three LiDAR measurements we considered in the previous section in Table 2.

From Equation 14, we can see that the contribution of horizontal heat transport to total heat transport is proportional to $(1 + c\Lambda)^{-2}$. As we discussed in the previous section, the correlation length for all data sets we considered is around $l_0 \approx 5.6$ m and is likely on the same order throughout the Arctic. This means that for ice of realistic thickness of around 1 m, $\Lambda \approx 5$. This implies that horizontal heat transport contributes less than 5% of the maximum possible contribution, $\Phi_h - \Phi_v$. This is very small—as we can see from Table 2, the total nondimensional flux, Φ, is equal to Φ_v to two significant digits for all measurements. Even for exceedingly thick ice of 2 m thickness, and snow with significant variability, as in the 2009N measurements, horizontal heat transport still contributes less than 1% of total ice growth. Therefore, horizontal heat transport can most likely be ignored on flat undeformed ice. This is in contrast with Sturm et al. (2002) who found a significant fraction of heat is transported horizontally in regions of deformed ice. For this reason, it may be necessary to include nonuniform ice thickness to appropriately capture heat transport on deformed ice.

Even though horizontal heat transport may be neglected on undeformed ice, snow variability may still noticeably contribute to conductive heat flux. In Table 2, we show the fraction, $(\Phi - \Phi_u)/\Phi$, of heat transport that is due to snow depth variability. We see that snow depth variability contributes between 4% for 2010 measurements that have the least snow depth variability and 11% for 2009N measurements that have the most snow depth variability, with the effect generally increasing with η and Σ. Although this is not large,

it is comparable to the effect of melt ponds during summer—for example, if 15% of ice of albedo 0.6 is covered by ponds of albedo 0.25, ice will melt on average 10% faster than if there were no ponds. Therefore, the effect of snow variability on first-year ice during winter may be enough to partially compensate the effect of melt ponds during summer. Again, this effect is smaller than on deformed ice, where Sturm et al. (2002) found that about a quarter of ice growth is due to variable snow and ice geometry.

We note that Equations 15 and 16, which quantify purely vertical and purely horizontal heat flux, follow from general properties of Laplace's equation in the limits $\Lambda \rightarrow \infty$ and $\Lambda \rightarrow 0$, and from the fact that the snow depth distribution is well described by a gamma distribution. These conditions do not change if we modify the "snow dune" model details such as mound shape, anisotropy, or size distribution (SI section S2.3), so our formula for total heat flux should be applicable regardless of such specifics. The only factor that could potentially change with these alterations is the detailed shape of the function that describes the transition between vertical and horizontal heat transport regimes.

Finally, we note that if a reasonable statistical model of spatial variability of snow conductivity can be developed, this variability could be included in the above framework. Namely, if snow has a nonconstant conductivity, $k_s(\mathbf{x})$, heat transport would be affected by an effective snow topography that accounts for these variations in conductivity, $h(\mathbf{x}) \frac{\langle k_s \rangle}{k_s(\mathbf{x})}$. Thus, a nonconstant snow conductivity would simply introduce an effective topography and, with a good statistical model of $k_s(\mathbf{x})$, we could follow the same steps to estimate the nondimensional heat fluxes, Φ, Φ_v, and Φ_h. We note that if the horizontal length scale of snow conductivity variations is on the order of, or less than, ice thickness, it could induce significant horizontal heat transport.

6. Melt Pond Evolution During Early Melt Season

During the early melt season, ice is largely impermeable and ponds can quickly flood vast areas of the ice surface. This is known as Stage I of pond evolution and is typically followed by Stages II and III which correspond to pond drainage and subsequent slow pond growth on highly permeable ice (Landy et al., 2014; Polashenski et al., 2012). In this section, we will discuss equations for pond evolution during Stage I when ice can be considered to be impermeable. We derive these equations in SI section S4. These equations follow from the fact that the premelt snow distribution on flat ice is well described by our "snow dune" topography.

6.1. Analytic Model for Pond Evolution During Stage I

Since water can flow relatively freely through permeable snow, during Stage I of pond evolution there likely exists a common water table for the entire ice floe, and ponds are the regions where surface topography lies below it. Therefore, to model Stage I of pond evolution, we will assume that snow is fully permeable and that snow below the water level is completely saturated with water, that underlying ice is impermeable and initially flat, that the premelt snow topography is well described by our "snow dune" model, and that no meltwater is lost from the domain (we will reconsider this assumption in the next subsection). The ice and snow topography can change by melting, thereby creating meltwater. We will thus assume that snow, bare ice, ponded ice, and ponded snow (water-covered snow) melt at different rates but that these rates are constant in space and time and independent of factors such as snow or pond depth. Finally, we will assume that both snow and ice melt only at the surface and that ice cannot melt until snow has melted away.

In SI section S4, we develop equations for the time evolution of pond coverage, p, and water level, w, during Stage I under the assumptions above. We do this by tracking the volume of water produced by melting. We use the fact that, if no water is lost from the domain, the water level can only increase, so that ponds only encounter bare snow topography that melts at a uniform rate and is, therefore, unaltered throughout the melt season. This means that we can use our premelt topography to accurately describe the ponded fraction of the surface. It also means that regions of bare ice (ice with no snow and no water on top) do not exist. We greatly simplify the problem by neglecting terms that are proportional to the density difference between water and ice, which are, in addition to being small, only relevant at very high pond coverage. Using this strategy, we show that pond coverage evolution is approximately the solution to the system of ordinary differential equations

$$\dot{w} \approx -\frac{r_i r_s (1-p)}{1 - r_s (1-p)} \dot{h}_s, \tag{17}$$

$$\dot{p} = f_\Gamma(w - \dot{h}_s t)(\dot{w} - \dot{h}_s), \tag{18}$$

where $\dot{x} \equiv \frac{dx}{dt}$ is a shorthand notation for the rate of change of quantity x, w is the water level, p is the pond coverage faction, $r_i \equiv \frac{\rho_i}{\rho_w}$ is the ratio of ice density to meltwater density, $r_s \equiv \frac{\rho_s}{\rho_i}$ is the ratio of snow density to pure ice density, $\dot{h}_s$ is the melt rate of bare snow, assumed to be constant in space and time and assumed to be negative since the height of the snow decreases with time, and $f_\Gamma(w - \dot{h}_s t)$ is the gamma distribution given by Equation 9 and evaluated at $w - \dot{h}_s t$. The parameters of the gamma distribution are determined from the mean and variance of the premelt snow topography according to Equation 10. The initial conditions for Equations 17 and 18 are no ponds at the initial time, $p(t=0)=0$, and a water level of 0, $w(t=0)=0$. Note that $\dot{h}_s < 0$, so $\dot{w} > 0$ and $\dot{p} > 0$. Even though Equations 17 and 18 are approximate, they are a very accurate approximation to the full 2-D model defined by the assumptions above at low pond coverage and only deviate slightly from the full model at high pond coverage (see SI section S4). In SI section S4, we also derive a second-order approximation that becomes nearly indistinguishable from the full 2-D model for any pond coverage.

We can see from Equations 17 and 18 that, since ice and water density are fixed, Stage I pond coverage evolution depends mainly on the density of snow through r_s, the melt rate of bare snow, $\dot{h}_s$, and the mean and variance of the initial snow depth distribution through f_Γ. Note that melt rates of bare ice, ponded ice, and ponded snow do not enter this first-order approximation for pond evolution. In Figures 5a–5d, we change each of the parameters that enter Equations 17 and 18 to see how they affect Stage I pond evolution. We note that in Figures 5a–5d, we parameterized f_Γ with its standard deviation, $\sigma(h)$, and its shape parameter, k, since $\sigma(h)$ strongly affects pond coverage evolution, while k affects it only weakly. Within a reasonable range of parameters, pond evolution during Stage I is most sensitive to the rate of snow melt (Figure 5a) and the standard deviation of the initial snow depth distribution (Figure 5c). In fact, as we explain in SI section S4, increasing the snow melt rate by some factor leads to the same pond coverage evolution as decreasing the volume of snow by the same factor. Snow density and the shape of the initial snow depth distribution, parameterized by k and assuming that $\sigma(h)$ is fixed, do not matter as much (Figures 5b and 5d).

6.2. Meltwater Drainage During Stage I

One important factor we have neglected is the potential for limited drainage during Stage I. Even though ice is typically impermeable during this stage, outflow pathways such as cracks in the ice, seal breathing holes, or the floe edge can exist (Eicken et al., 2002; Fetterer & Untersteiner, 1998; Holt & Digby, 1985; Polashenski et al., 2012). Popović et al. (2020) explain that if pond coverage is low, and the underlying surface is impermeable, such isolated flaws in the ice should not significantly affect the pond coverage. However, if pond coverage is above a special value called the percolation threshold, p_c, there can be significant pond drainage through these flaws. In fact, if the drainage rate is great enough, the pond coverage would be limited to below p_c. For example, unless ice deformation prevents water from flowing into the ocean, the floe edge will limit pond growth to below p_c. Popović et al. (2018, 2020) estimate p_c to be between 0.3 and 0.4 for Arctic sea ice. Below, we show that including drainage is necessary to accurately reproduce the evolution of pond coverage throughout Stage I.

Including drainage in our model leads to some inconsistencies with the assumptions under which we derived Equations 17 and 18. First, drainage opens the possibility for the water level to decrease, $\dot{w} < 0$, potentially exposing bare ice and topography that was altered by different melt rates of different regions of ice. These effects were not taken into account when deriving Equations 17 and 18, and, therefore, we can keep these equations only if the drainage is not too great. In fact, Equations 17 and 18 remain valid when $\dot{w} - \dot{h}_s > 0$ (the altered topography remains submerged) and while $w > 0$ (there are no regions of bare ice). Second, the percolation threshold only affects the pond coverage in the way we discussed above if the underlying surface is impermeable. In our case, the surface is a combination of impermeable ice and permeable snow. Since the pond coverage will likely exceed the percolation threshold before all the snow melts, there likely exists a
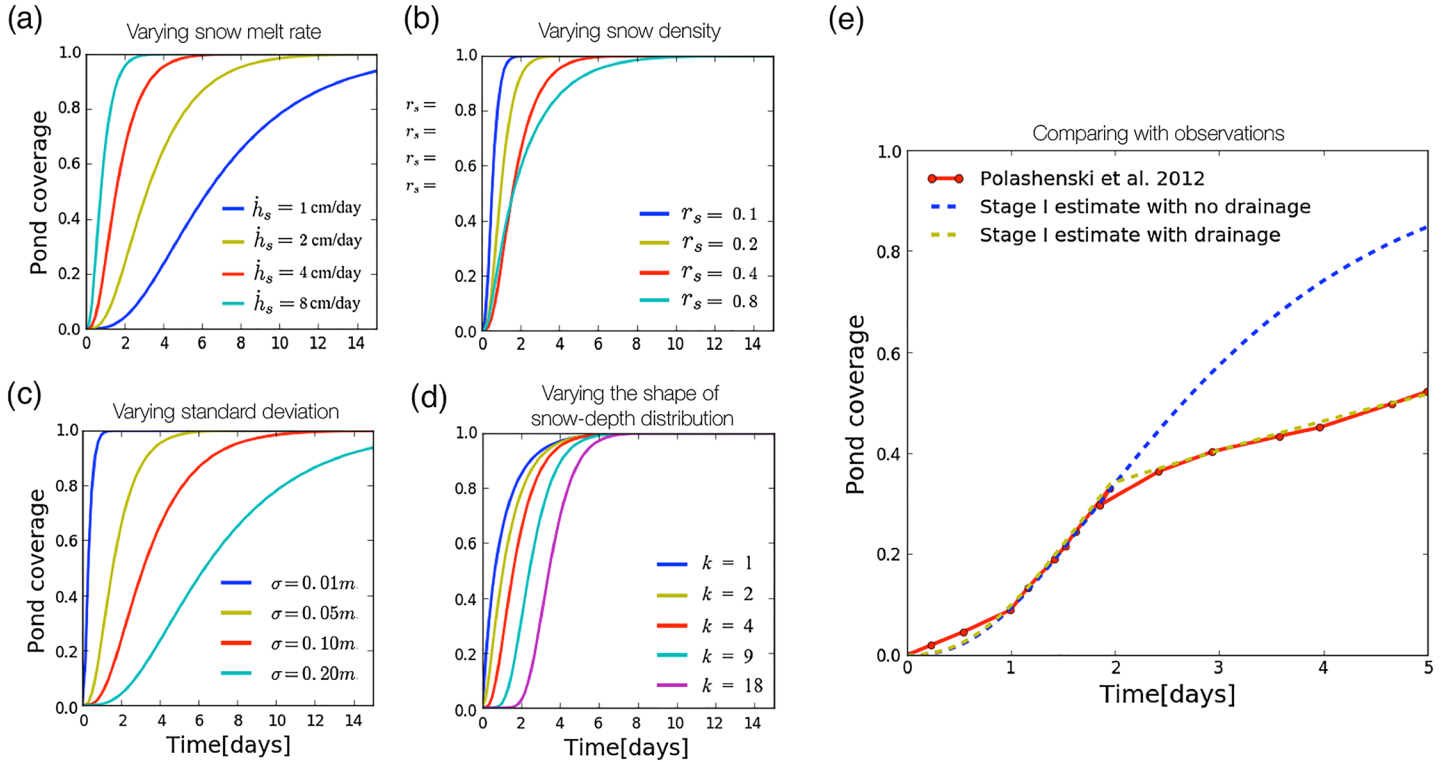
Figure 5. (a–d) Pond coverage evolution during Stage I found using Equations 17 and 18 for a variety of model parameters. In each panel, we change one parameter, while we keep the others fixed at default values $\dot{h}_s = 4$ cm day^{-1}, r_s=0.4, $\sigma(h)$=0.05 m, and k=4. (a) Pond coverage evolution for different snow melt rates, $\dot{h}_s$. (b) Pond coverage evolution for different snow to ice density ratios, r_s. (c) Pond coverage evolution on topographies with different snow depth standard deviations, $\sigma(h)$. (d) Pond coverage evolution on topographies with different shape parameters, k. (e) Comparing pond evolution during Stage I calculated using Equations 17–19 and physical parameters described in the text (dashed blue and yellow lines) with observations of Polashenski et al. (2012) (red line). The dashed blue line represents pond evolution estimated using Equations 17 and 18 that assumes no drainage during Stage I. Dashed yellow line represents pond evolution estimated using Equation 19, which assumes a constant drainage rate beyond the percolation threshold of p_c=0.35. Topography used to calculate Stage I evolution has the same mean and variance as the actual measured premelt snow topography obtained with LiDAR measurements.

complicated transition period between a surface that is a mix of permeable snow and impermeable ice and a fully impermeable ice surface. Moreover, when drainage is great enough so that the percolation threshold limits pond growth, the water level in different ponds needs to be at least slightly different, in contrast with the assumption of a common water table we made in the previous subsection. Here, we simply ignore these complications and assume that Equations 17 and 18 are approximately valid even when pond drainage occurs and that drainage is only activated if pond coverage exceeds the percolation threshold. We leave a detailed analysis of pond drainage during Stage I for another study.

If we assume $\dot{w} - \dot{h}_s > 0$ and $w > 0$, we can straightforwardly include drainage in pond evolution (Equations 17 and 18) by simply altering the water balance equation. We derive this in SI section S4. For example, if ponds drain at a rate of Q cm per day, Equation 18 remains the same and 17 is modified to

$$\dot{w} = -\frac{r_i r_s (1-p)\dot{h}_s + Q}{1 - r_s(1-p)}. \tag{19}$$

To account for the fact that we expect little drainage to occur below the percolation threshold, we can make Q a function of p. The simplest representation would be to include $Q(p) = Q_0 \mathcal{H}(p - p_c)$, where $\mathcal{H}$ is the Heaviside function, equal to 0 or 1 depending on whether its argument is less or greater than 0, and Q_0 is

a constant that sets the maximum drainage rate. Using this function yields the yellow line in Figure 5e. If $\dot{w} - \dot{h}_s < 0$, Equation 18 predicts that the pond coverage will decrease, $\dot{p} < 0$. So, if $\dot{w} < \dot{h}_s$, we expect the pond coverage to remain fixed at the percolation threshold, $p = p_c$.

In Figure 5e we compare Stage I pond evolution predicted by our model with the measurements of Stage I pond coverage evolution by Polashenski et al. (2012). Since accurate measurements of premelt topography are available for that time and location (Figure 3), we can choose the parameters of the gamma distribution highly accurately. The density of snow and the snow melt rate are somewhat uncertain. We choose the density of snow to be $\rho_s = 350\ \mathrm{kg\ m^{-3}}$, and the albedo of melting snow to be $\alpha_s = 0.74$, consistent with observations of Polashenski et al. (2012). We take the solar flux to be $F_{\mathrm{sol}} = 254\ \mathrm{W\ m^{-2}}$, which Polashenski et al. (2012) report as the average flux of solar energy for the duration of the experiment. We treat the sum of long-wave, sensible, and latent heat fluxes, F_r, as a tuning parameter. The value we choose, $F_r = -15\ \mathrm{W\ m^{-2}}$, is typical of the region and season, and is therefore consistent with the measurements. The blue line in Figure 5e shows the Stage I pond evolution predicted by Equations 17 and 18, while the red line represents the measurements of Polashenski et al. (2012). The two curves agree up to the point when pond coverage reaches $p \approx 0.35$, a plausible value for the percolation threshold. Thus, the measurements are consistent with drainage being activated beyond the percolation threshold. To match pond evolution beyond $p = 0.35$ we used Equation 19, and tuned the drainage rate, Q_0, to 2.6 cm day^{-1} (yellow line), a rate consistent with observations of Polashenski et al. (2012). We can see that Equation 19 is consistent with the observations, although this matching cannot be fully confirmed due to uncertainty in the parameters.

6.3. A Condition for Pond Development

Pond coverage reaches its peak by the end of Stage I. Afterward, ponds drain, and, by the end of the drainage stage, the remaining ponds correspond to regions of ice that are below sea level. Observations show that ponds that remain after drainage are a subset of ponds that exist during peak pond coverage (Landy et al., 2014; Polashenski et al., 2012). Therefore, if ponds do not develop during Stage I, they will likely never develop. Since the premelt snow depth distribution controls pond evolution during Stage I, it, therefore, also has a disproportionate effect on later pond evolution. If the snow depth is highly variable, ponds will develop sooner than if the snow cover is uniform. If the snow cover is relatively uniform and Stage I does not last long enough, the ice may remain pond-free throughout the summer. Here, we will show how we can use the model we developed above to derive a simple criterion for whether ice will develop ponds or not.

We start with Equations 17 and 18. If we assume that pond coverage stays low throughout Stage I, we can set $p \approx 0$ in Equation 17, and integrate it directly to get the water level at time t during Stage I, $w(t) \approx -\dfrac{r_i r_s}{1 - r_s}\,\dot{h}_s t$.

We can then nondimensionalize Equation 18 by introducing nondimensional parameters Σ and ω to get

$$\frac{\mathrm{d}p}{\mathrm{d}\omega} = \widetilde{f}_\Gamma(\omega,\ \Sigma), \tag{20}$$

$$\Sigma \equiv \frac{\sigma(h)}{\langle h \rangle}, \qquad \omega \equiv -\frac{1 - r_s(1 - r_i)}{1 - r_s}\frac{\dot{h}_s t}{\langle h \rangle}, \tag{21}$$

Here, Σ is the nondimensional roughness as in section 5 and ω can be interpreted as a nondimensional water level. As in Equation 15 of section 5, $\widetilde{f}_\Gamma(\omega,\ \Sigma)$, is a gamma distribution with a mean equal to 1, so that it only depends on Σ, with parameters $k = \Sigma^{-2}$ and $h_0 = \Sigma^2$, and evaluated at ω. Thus, from Equation 20, we get a simple relation

$$p = F_\Gamma(\omega,\ \Sigma), \tag{22}$$

where $F_\Gamma(\omega,\ \Sigma)$ is a cumulative gamma distribution with a mean equal to 1, $F_\Gamma(\omega,\ \Sigma) \equiv \int_0^\omega \widetilde{f}_\Gamma(z,\ \Sigma)\mathrm{d}z$. Therefore, if pond coverage is low, it depends only on ω and Σ and we can express it simply in terms of the cumulative gamma distribution.

Let us now assume that Stage I lasts for some time, T, on the order of 5 days. If the ponds do not develop within that time, the ice will remain pond-free throughout the summer. We can set some threshold, p^*,

Non-dimensional snow roughness and water level determine the extent of pond development
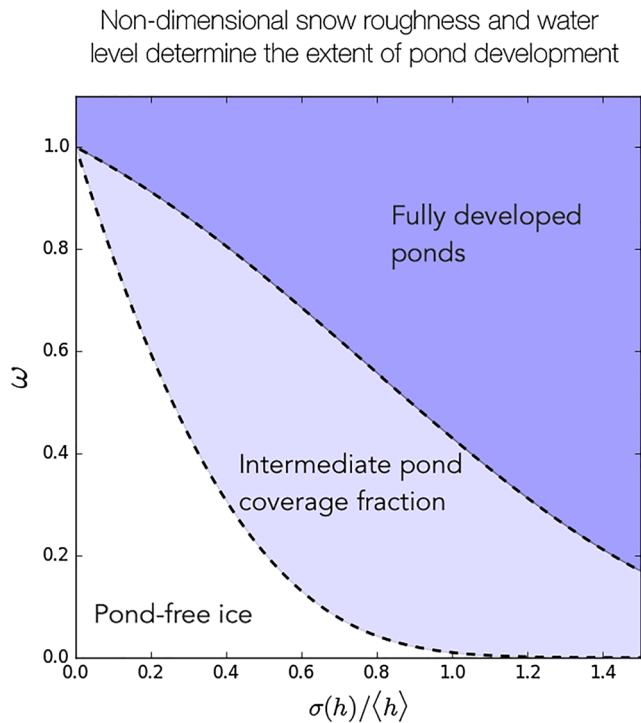
Figure 6. The horizontal axis shows the nondimensional snow roughness, $\sigma(h)/\langle h \rangle$, while the vertical axis shows the nondimensional water level, ω, described in the text. The white region represents ice that remains pond-free throughout the summer, while the dark-blue region represents ice that develops pond coverage that exceeds the percolation threshold by the end of Stage I. The light-blue region represents ice that has some ponds by the end of Stage I, but the pond coverage does not exceed the percolation threshold.

say $p^* = 0.01$, and consider ice to be pond-free if the pond coverage is below p^*. We can then find the boundary in $\omega-\Sigma$ space, $\omega^*(\Sigma)$, such that if $\omega<\omega^*$, ice remains pond-free at the end of Stage I. According to Equation 22, this boundary is given by

$$\omega^*(\Sigma) = F_\Gamma^{-1}(p^*, \Sigma), \qquad (23)$$

where F_Γ^{-1} is an inverse of the cumulative gamma distribution (gamma percentile function) with a mean equal to 1, $k = \Sigma^{-2}$, and $h_0 = \Sigma^2$, evaluated at p^*. Equation 23 gives a universal criterion that ice remains pond-free. If ω, calculated given the snow melt rate, density, depth, roughness, and the duration of Stage I, exceeds ω^*, ice will develop at least some ponds. The boundary, $\omega^*(\Sigma)$, is largely insensitive to the choice of the threshold coverage, p^*, so long as p^* is much smaller than 1.

In the case when ice develops some ponds, we can also ask how developed those ponds will be. In particular, we can assume that ponds are fully developed if the pond coverage exceeds the percolation threshold by the end of Stage I. Beyond the percolation threshold, pond drainage likely starts to play an important role, and the post-Stage I evolution of fully developed ponds likely proceeds in a fairly typical manner. Therefore, there likely exist three typical trajectories for pond evolution during summer—pond-free, fully developed, and intermediate. To see whether the ponds will develop fully, we can again use Equation 23 but use $p^* = p_c \approx 0.35$. Using Equation 23 with $p^* = 0.35$ is approximate since the pond coverage is no longer small, but it is still reasonably accurate.

In Figure 6, we show the conditions for these three regimes of pond development. We can see that when $\omega > 1$, ponds always fully develop since, in this case, the water level by the end of Stage I exceeds the height of snow even when the snow cover is uniform. Otherwise, if $\omega<1$, ponds develop more easily when the snow depth has more variability. We can estimate ω and Σ for the measurements of Polashenski et al. (2012). We use $T = 5$ days, snow depth mean and variance estimated from the LiDAR measurements, and the same snow melt rate density as in the previous subsection. We show Σ and ω estimated in this way in Table 2. We can see that $\omega > 1$ in all cases so that we expect that ponds develop fully. In the study of Polashenski et al. (2012) this indeed happened. In order for ice to have remained pond-free, Stage I would have had to have lasted less than 1.5 days in 2010, which had the most uniform snow, and less than 0.5 days for 2009N, which had the most variable snow. We note that persistently pond-free ice has been observed in the Arctic (Perovich et al., 2002), while Antarctic sea ice only rarely develops ponds. Although we do not have snow measurements from these pond-free ice floes, general conditions on Antarctic ice are broadly consistent with our framework here. Snow on Antarctic ice is typically deeper than in the Arctic, lowering both Σ and ω, and it is both thinner and more saline than Arctic ice, potentially lowering the duration of Stage I, T, thereby further lowering ω. It would be interesting to see where these pond-free ice floes fall within our pond development diagram.

7. Discussion

Throughout this paper, we showed that our model can reproduce key statistical features on three nearby locations where detailed LiDAR data were collected as well as two other locations where melt pond images were taken. Although this is not enough to claim generality, our results are encouraging, suggesting that our model may be applicable in large-scale studies of snow on undeformed Arctic sea ice and could serve as a starting point for studying snow on other terrains such as deformed ice, Antarctic ice, or Alpine snow fields. Moreover, as the fraction of first-year ice increases in the Arctic due to global warming, the conditions similar to the ones we tested here will likely become more common. Here, we will briefly discuss how our results can be applied to large-scale studies, assuming their generality holds.

1. We believe that large-scale models should use a gamma distribution for snow depth on undeformed ice. Even though other distributions, such as normal or lognormal, may still work well enough, adopting a gamma distribution is a more principled approach that likely works over a wider range of parameters. Therefore mean and variance of snow depth are enough to characterize the whole distribution according to Equations 10. Since, according to the LiDAR as well as melt pond data, the correlation length appears to be stable under a variety of environmental conditions, it may be possible to use our "snow dune" model with a horizontal scale parameter $r_0 = 0.6$ m ($l_0 = 5.6$ m) to study horizontal snow distribution.

2. When modeling heat conduction through undeformed ice, it is likely safe to neglect horizontal heat transport. On deformed ice, the situation may be more complicated and further study is required.

3. To parameterize ice albedo during summer, Equations 17 and 18 may be used for pond evolution during Stage I. Without knowing the outflow rate, Q, a reasonable approach would be to cap pond coverage to below the percolation threshold of 0.3 to 0.4. Equations 17 and 18 can be combined with similar approaches, such as the model of Popović et al. (2020) for Stages II and III, or the model of Popović et al. (2018) for Stage III, to yield an analytic and accurate model of pond evolution throughout the entire melt season.

4. Equation 23 provides a yet untested prediction of whether ice will remain pond-free throughout the summer—we were not able to test this criterion against real data appropriately, as in all three cases we considered, the ponds have fully developed. So, it would be interesting to see whether this criterion can explain the observations of pond-free ice in the Arctic and the Antarctic. The nondimensional water level, ω, in Equation 23 depends on the duration of Stage I. So, to be able to use this equation in large-scale studies, it will be necessary to relate the duration of Stage I to parameters that are available on the large scale, such as energy fluxes, thickness, or the salinity of ice.

8. Conclusions

Snow cover greatly impacts sea ice evolution. It insulates the ice during the winter, reflects sunlight during the summer, and controls melt pond evolution. In this paper, we presented an idealized geometric model of "snow dune" topography that was capable of capturing key statistical properties of the snow cover on undeformed first-year sea ice on three sites for which detailed LiDAR measurements were available as well as for two other missions that collected airborne melt pond images. The main conclusion of our paper is that, at least for the measurements we considered, our "snow dune" model is a very accurate representation of the three-dimensional snow distribution on flat, undeformed Arctic sea ice.

By comparing the moments of the height and snow depth distributions, we showed that the height distribution of our model is statistically indistinguishable from the snow depth distribution measured in detailed LiDAR scans on flat undeformed ice. We also compared the correlation functions for the model and the measurements to show that the horizontal statistics of snow are also well captured by our model. In addition to this, our model captures melt pond geometry derived from helicopter images that span areas of 1 km^2 with the same model parameters as the LiDAR scans. This suggests that our model may capture the horizontal properties of snow on such large scales. We note that in all cases we tested, the correlation length of horizontal features (either snow or melt pond), was around $l_0 \approx 5.6$ m, suggesting that this property may be constrained throughout the Arctic. Since our model is fully defined by only three parameters, it follows that it is enough to know the mean snow depth, its variance, and the horizontal correlation length to fully characterize the statistics of snow on undeformed ice. On ice that was slightly deformed, we showed that the measured snow depth distribution contains subtle differences from our model and that there exist long-range correlations in the horizontal, inconsistent with our model.

After comparing our "snow dune" model to measurements, we considered its application to heat conduction through the ice and to the development of melt ponds. We solved a three-dimensional heat conduction equation assuming the ice is flat and the snow cover is well described by our model. We developed simple formulas that solve the conductive heat flux problem for any configuration of snow consistent with our model. Using these formulas, we showed that, for any realistic ice thickness and snow dune size, horizontal heat transport may be neglected on flat, undeformed ice (although this may not be the case for deformed ice). We then also used our model to develop a simple model for melt pond evolution during early stages of pond development when ice can be considered impermeable. We found that pond coverage evolution can be

estimated using a system of two coupled ordinary differential equations that closely approximate an equivalent 2-D model, but are much simpler to solve. They reveal connections with measurable environmental parameters. For example, we show that doubling the amount of solar radiation has approximately the same effect on pond growth rate as halving the snow depth. We also show that these equations are consistent with observations. Using these equations, we develop a criterion in terms of nondimensional properties of the ice surface for whether ice will develop ponds or remain pond-free during summer.

In this paper, we demonstrated that many of the details of ice surface conditions can be summarized by only a few parameters if one is interested in bulk properties such as the total heat conducted or the mean melt pond coverage. Of the three parameters that define our model, it may be the case that only two change from situation to situation, as the correlation length may be stable, as discussed above. This means that future GCMs may need to only keep track of the total amount of snow and the snow depth variance in order to be able to represent the snow surface in a principled way. Our results, therefore, uncover an important property of sea ice snow cover that may improve the realism of sea ice models while adding little to their complexity.

Conflict of Interest

The authors declare no conflict of interest.

Data Availability Statement

Code to generate the synthetic "snow dune" topography is archived as Popović (2020) and is also available online (at https://github.com/PedjaPopovic/Snow-dune-topography). LiDAR measurements collected by Polashenski et al. (2012) are available for download (at https://chrispolashenski.com/data.php or https://data.eol.ucar.edu/dataset/106.426).

References

Eicken, H., Krouse, H. R., Kadko, D., & Perovich, D. K. (2002). Tracer studies of pathways and rates of meltwater transport through Arctic summer sea ice. *Journal of Geophysical Research*, *107*(C10), 8046. https://doi.org/10.1029/2000JC000583

Fetterer, F., & Untersteiner, N. (1998). Observations of melt ponds on Arctic sea ice. *Journal of Geophysical Research*, *103*(C11), 24,821–24,835.

Filhol, S., & Sturm, M. (2015). Snow bedforms: A review, new data, and a formation model. *Journal of Geophysical Research: Earth Surface*, *120*, 1645–1669. https://doi.org/10.1002/2015JF003529

Holland, M. M., & Curry, J. A. (1999). The role of physical processes in determining the interdecadal variability of central Arctic sea ice. *Journal of climate*, *12*(11), 3319–3330.

Holt, B., & Digby, S. A. (1985). Processes and imagery of first-year fast sea ice during the melt season. *Journal of Geophysical Research*, *90*(C3), 5045–5062.

Kochanski, K., Anderson, R. S., & Tucker, G. E. (2019). The evolution of snow bedforms in the Colorado Front Range and the processes that shape them. *The Cryosphere*, *13*(4), 1267–1281.

Kochanski, K., Defazio, G.-C., Green, E., Barnes, R., Downie, C., Rubin, A., & Rountree, B. (2019). Rescal-snow: Simulating snow dunes with cellular automata. *Journal of Open Source Software*, *4*(42), 1699.

Landy, J., Ehn, J., Shields, M., & Barber, D. (2014). Surface and melt pond evolution on landfast first-year sea ice in the Canadian Arctic Archipelago. *Journal of Geophysical Research: Oceans*, *119*, 3054–3075. https://doi.org/10.1002/2013JC009617

Liston, G. E., Polashenski, C., Rösel, A., Itkin, P., King, J., Merkouriadi, I., & Haapala, J. (2018). A distributed snow-evolution model for sea-ice applications (snowmodel). *Journal of Geophysical Research: Oceans*, *123*, 3786–3810. https://doi.org/10.1002/2017JC013706

Mather, K. B. (1962). Further observations on sastrugi, snow dunes and the pattern of surface winds in Antarctica. *Polar Record*, *11*(71), 158–171.

Perovich, D. K. (1996). The optical properties of sea ice (Tech. Rep.). Cold Regions Research and Engineering Lab Hanover NH.

Perovich, D. K., & Richter-Menge, J. A. (2009). Loss of sea ice in the Arctic. *Annual Review of Marine Science*, *1*, 417–441.

Perovich, D. K., Tucker, W. B., & Ligett, K. A. (2002). Aerial observations of the evolution of ice surface conditions during summer. *Journal of Geophysical Research*, *107*(C10), 8048. https://doi.org/10.1029/2000JC000449

Petrich, C., Eicken, H., Polashenski, C. M., Sturm, M., Harbeck, J. P., Perovich, D. K., & Finnegan, D. C. (2012). Snow dunes: A controlling factor of melt pond distribution on Arctic sea ice. *Journal of Geophysical Research*, *117*, C09029. https://doi.org/10.1029/2012JC008192

Polashenski, C., Golden, K. M., Perovich, D. K., Skyllingstad, E., Arnsten, A., Stwertka, C., & Wright, N. (2017). Percolation blockage: A process that enables melt pond formation on first year Arctic sea ice. *Journal of Geophysical Research: Oceans*, *122*, 413–440. https://doi.org/10.1002/2016JC011994

Polashenski, C., Perovich, D., & Courville, Z. (2012). The mechanisms of sea ice melt pond formation and evolution. *Journal of Geophysical Research*, *117*, C01001. https://doi.org/10.1029/2011JC007231

Popović, P. (2020). *PedjaPopovic/Snow-dune-topography: Code to create an artificial 'snow dune' topograhy*. Switzerland: Zenodo. Retrieved from https://doi.org/10.5281/zenodo.3930517

Popović, P., Silber, M., & Abbot, D. (2020). Critical percolation threshold restricts late-summer Arctic sea ice melt pond coverage. *Journal of Geophysical Research: Oceans*, *125*, e2019JC016029. https://doi.org/10.1029/2019JC016029

Popović, P., Cael, B. B., Silber, M., & Abbot, D. S. (2018). Simple rules govern the patterns of Arctic sea ice melt ponds. *Physical review letters*, *120*(14), 148701.

Sharma, V., Braud, L., & Lehning, M. (2019). Understanding snow bedform formation by adding sintering to a cellular automata model. *The Cryosphere*, *13*(12), 3239–3260.

Stroeve, J., Holland, M. M., Meier, W., Scambos, T., & Serreze, M. (2007). Arctic sea ice decline: Faster than forecast. *Geophysical research letters*, *34*, L09501. https://doi.org/10.1029/2007GL029703

Sturm, M., Perovich, D. K., & Holmgren, J. (2002). Thermal conductivity and heat transfer through the snow on the ice of the Beaufort Sea. *Journal of Geophysical Research*, *107*(C10), 8043. https://doi.org/10.1029/2000JC000409

Untersteiner, N. (1964). Calculations of temperature regime and heat budget of sea ice in the central Arctic. *Journal of Geophysical Research*, *69*(22), 4755–4766.

Yen, Y.-C. (1981). Review of thermal properties of snow, ice and sea ice: Cold Regions Research and Engineering Lab Hanover NH.